Antimicrobial Combination Effects at Sub-inhibitory Doses do not Reliably Predict Effects at Inhibitory Concentrations

Malte Muetter[1,✉], **Daniel Angst**[1], **Roland Regoes**[1], **and Sebastian Bonhoeffer**[1,✉]

[1]Department of Environmental Systems Science, ETH Zürich, Universitätstrasse 16, 8092 Zürich, Switzerland

Assessing whether drug combinations synergise or antagonise is difficult for several reasons: (i) measuring bacterial death rates at clinically relevant drug concentrations is methodologically challenging, (ii) there is no unifying definition of what constitutes synergistic or antagonistic interactions, and (iii) both synergism and antagonism may be concentration and mixing ratio dependent. To assess how well sub-inhibitory measurements predict inhibitory behaviour, we quantified drug interactions for 15 pairwise drug combinations on a concentration checkerboard covering a wide range of inhibitory and sub-inhibitory concentrations. To this end, we recorded 8640 time-resolved luminescence trajectories that have been shown to track bacterial population declines. To handle time-varying treatment effects and allow fair comparisons between drugs with distinct killing dynamics, we introduced a growth-integrated rate-like metric ψ to summarise each trajectory, and assigned interaction types (synergistic/independent/antagonistic) based on Bliss independence and Loewe additivity. We found that the interaction type frequently changes as the concentration increases from sub-inhibitory to inhibitory concentrations. Moreover, interaction type depended on the mixing ratio, implying that single-point sub-inhibitory measurements are not sufficient to predict interactions at clinically relevant concentrations.

antibiotic combinations, dose-dependence, drug interactions, pharmacodynamics, time-variant treatment effects

Correspondence: ***science@maltemuetter.ch, seb@env.ethz.ch***

Introduction

Antimicrobial resistance (AMR) poses a major global health burden, with an estimated 1.14 million deaths directly attributable to resistant infections in 2021 alone [1]. Moreover, the lag between the introduction of a new antibiotic class and the emergence of clinical resistance appears to be shrinking [2]. To develop a more sustainable approach to antibiotic use, a deeper understanding of the influence of treatment on the evolution of resistance is necessary.

One strategy that has been shown to slow the evolution of resistance in notoriously fast-evolving pathogens, such as HIV, malaria, and tuberculosis, is combination therapy [3, 4]. In theoretical models, combination therapy seems to outperform other strategies (such as mixing or cycling) [5–7], and it also seems to perform best in in vitro simulations of epidemics [8, 9]. However, clinical evidence for the efficacy of combination therapy is inconclusive, and a comprehensive meta-analysis did not identify a significant overall benefit [10].

Several factors contribute to the inconclusiveness of clinical studies, ranging from ethical constraints that limit focal pathogens to comparatively benign ones (i.e. excluding HIV and *M. tuberculosis*) to the lack of statistical power to track resistance evolution [10]. Another potential reason is drug interactions. Drug combinations can exhibit synergistic or antagonistic interactions, depending on whether the combined effect is stronger or weaker than the expectation based on the effects of the single drugs. However, defining this expectation is non-trivial, as null models are numerous and the best choice to describe drug independence remains debated [11, 12]. Here, we use two classical and widely applied reference frameworks to define independence: the response-based Bliss independence [13] and dose-based Loewe additivity [14].

Bliss independence is based on the assumption that the probability of being affected by one drug is statistically independent of being affected by the other [13]:

$$p_{AB}^{\text{Bliss}} = p_A + p_B - p_A\, p_B. \tag{1}$$

Under this assumption, Bliss independence is expected to be more appropriate for drug pairs with distinct and non-overlapping mechanisms of action [15].

In contrast, Loewe additivity – first discussed as iso-additivity by Frei in 1913 [16] and later formalised by Loewe and Muischnek [14] – uses dose equivalence as a null model. A combination is considered additive if pairs of concentrations that produce the same effect ψ (i.e. a measure of net growth) lie on a linear isobole connecting the equivalent single-drug doses [14]:

$$\frac{c_A}{f_A^{-1}\big(\psi(c_A, c_B)\big)} + \frac{c_B}{f_B^{-1}\big(\psi(c_A, c_B)\big)} = 1. \tag{2}$$

Here f_i^{-1} represents the inverse of a pharmacodynamic function $f_i(c)$ that maps drug concentrations c_i to an effect measure ψ.

There are many studies on drug interactions below the minimum inhibitory concentration (MIC) (e.g. [17–25]) and at the MIC level (e.g. [26–28]). However, studies covering the arguably clinically more relevant inhibitory regime are scarce and often cover only a few points in the inhibitory range (e.g. [29–33]). The primary reason for this is methodological: under sub-inhibitory conditions, growth rates can be easily assessed at high throughput using optical density measurements, whereas inhibitory conditions typically require

labour-intensive, low-throughput colony-forming unit assays [34]. This lack of data on effects at high concentrations is a problem, not only because inhibitory conditions are more relevant therapeutically, but also because the right, inhibitory, tail of the pharmacodynamic curve has a strong influence on resistance evolution [35].

It has already been shown that drug interactions can depend on dose and mixing ratio [18, 23, 36–38]. However, the existing literature provides limited quantitative insight into how frequently interaction classifications remain stable versus how often they change with concentration and mixing ratio. Here, we provide an extensive map of interactions for 15 antibiotic pairs, each measured on a 12×12 concentration checkerboard that includes inhibitory concentrations using time-resolved bioluminescence trajectories. We quantify how often sub-inhibitory interaction classifications based on Bliss independence and Loewe additivity generalise to inhibitory conditions and how often they fail, including cases of qualitative reversals across regimes.

Results

We quantified drug interactions for 15 pairwise combinations of six antibiotics falling into three mechanistic classes: polymyxins (colistin, COL; polymyxin B, POL), β-lactams (amoxicillin, AMO; penicillin, PEN), and ribosome-targeting drugs (chloramphenicol, CHL; tetracycline, TET). For each drug pair, we assessed 144 conditions (c_A, c_B) in a 12×12 checkerboard. We measured light intensity trajectories $I(t)$ for 8,640 bioluminescent cultures to infer changes in population size over time. Single-drug trajectories are shown in Figure S1.

Time-variant growth rates and treatment effects. Most drug-interaction metrics are based on estimates of *treatment effects*, which collapse the trajectories of the bacterial population size into a scalar. These estimates are typically either rate-based, obtained by fitting an exponential rate of change to a growth trajectory [17, 31, 39–41], or area under the curve (AUC)-based, obtained by integrating a (transformed) growth trajectory over time [24, 30, 32, 33, 42, 43]. Rate-based approaches are easy to interpret and can be used directly in epidemiological models. However, slopes are sensitive to the choice of the fitting window when treatment effects are time-variant. This sensitivity is especially problematic when assessing interactions among drugs with very different killing dynamics (e.g., in the example shown in Figure 1a), where treatment effects start at different time points and persist for different durations.

Given that many trajectories exhibited time-varying treatment effects, we summarised each trajectory by ψ (Methods), a time-weighted average of the instantaneous net growth rate $\hat{\psi}(t)$ (Equation S1). This weighting emphasises early treatment effects, reflecting that early changes in net growth shape the population for a longer duration than equally sized changes occurring later. ψ is proportional to the area under the log-normalised luminescence trajectory $Y(t) = \ln(I(t)/I(0))$ (Equation S3). Treatment effects, τ, are then

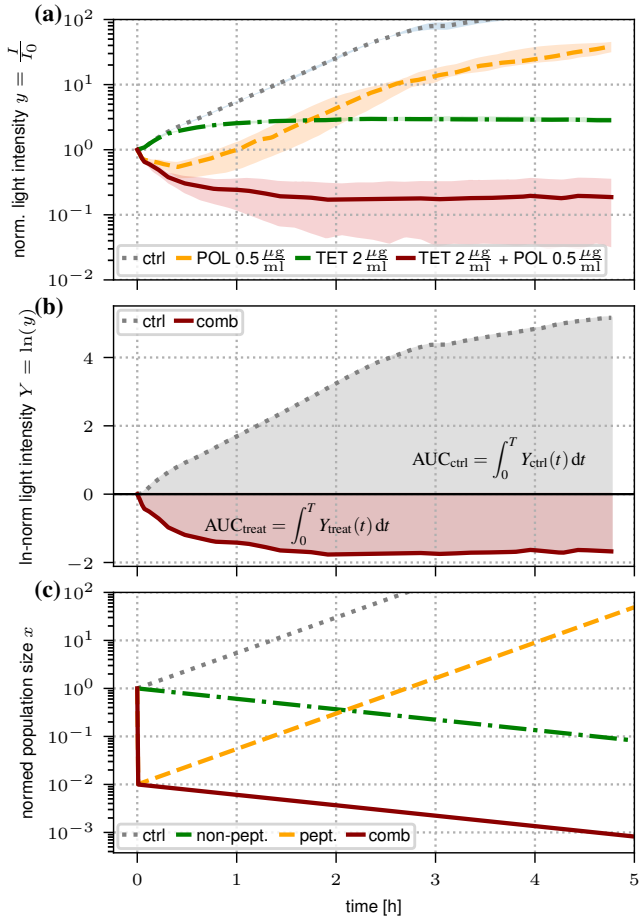

Figure 1: Panel (a) shows the median of normalised light-intensity trajectories $y(t) = I(t)/I(0)$ for the combination of polymyxin B (POL, $0.5\,\frac{\mu g}{mL}$) and tetracycline (TET, $2\,\frac{\mu g}{mL}$), together with the corresponding single-drug and untreated control trajectories, with shaded bands indicating the interquartile range across biological replicates. Panel (b) shows the log-transformed signal $Y(t) = \ln(y(t))$ for the untreated control and the combination treatment from panel (a), together with their associated areas under the curve. Panel (c) shows a simple peptide–antibiotic interaction model illustrating qualitatively distinct dynamics under: no drugs, antibiotic (slow constant decline), peptide (rapid initial decline), and peptide plus antibiotic (rapid initial decline followed by a constant slow decline).

defined as the difference between the time-weighted net growth rates of an untreated control and the treated condition, and correspond to the scaled area between curves (Figure 1b). Time-weighted net growth rates for one example (CHL+TET) are shown in Figure 2, with markers indicating conditions as inhibitory (stars), sub-inhibitory (diamonds), or intermediate (no marker). Rates for all conditions are shown in Figure S3. For further details see Methods. We then fitted pharmacodynamic curves to the single-drug estimates (Figure S2).

For each condition (c_A, c_B) we estimate the bootstrap distribution $\boldsymbol{\tau}(c_A, c_B)$ by resampling pairs of control and treatment wells with replacement (Methods, subsection 1G). Throughout this manuscript, we denote distributions with bold symbols. For each bootstrap draw b, we compute $\tau_b(c_A, c_B) = \psi_b(\emptyset) - \psi_b(c_A, c_B)$.

Bliss independence implies additive treatment effects. Because the original Bliss formulation is probabilistic, we have to translate it into our growth-based treatment-effect

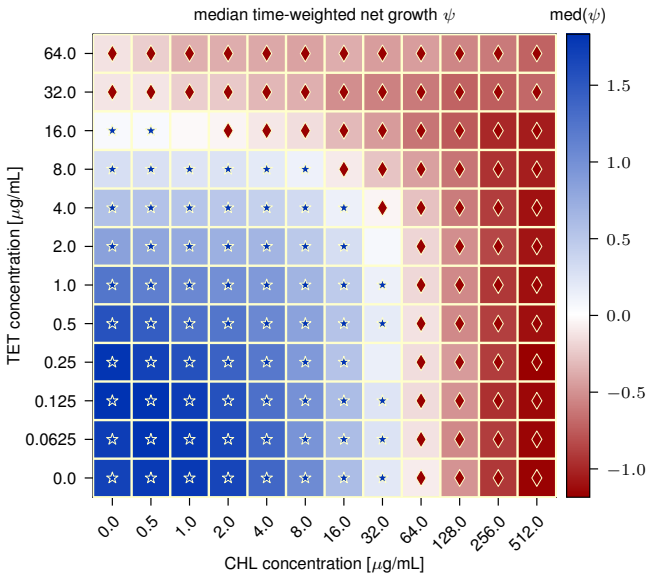

Figure 2: Time-weighted growth rate ψ for combinations of CHL and TET. Each cell corresponds to one concentration pair, with colour indicating the median of ψ across $n = 4$ biological replicates. Markers denote whether the distribution of ψ is significantly different from zero (see Methods): stars indicate significantly positive values (net growth), and diamonds indicate significantly negative values (net killing).

framework (see SI 1D). Bliss independence implies multiplicative survival $S_{AB}(T) = S_A(T)\,S_B(T)$ (Equation S12). After substituting $S_i(T) = \exp\big(-\int_0^T \hat{\tau}_i(u)\,du\big)$ with $\hat{\tau}_i(t)$, denoting the *instantaneous treatment effect*, we can derive that Bliss implies additive *time-weighted treatment effects*:

$$\tau^{\text{Bliss}}(c_A, c_B) = \tau(c_A) + \tau(c_B). \tag{3}$$

Peptide – non-peptide interaction model. We observed that a combination of non-peptide drugs with relatively constant inhibition dynamics and peptide-like drugs, which induce a sharp early decline followed by (almost) unimpaired growth, is dominated by the peptide drug in the early phase and by the non-peptide drug in the later phase. A well-behaved example of such a combination is shown in Figure 1a for polymyxin B (POL) and tetracycline (TET). Because most interaction metrics do not explicitly account for time-varying effects, it is unclear what combined treatment effect to expect. To answer this, we constructed a mathematical model for an idealised scenario. Drug A immediately reduces the population by a factor α but does not affect the subsequent dynamics, while drug B acts invariantly over time by constantly reducing the net growth rate from $\hat{\psi}_{\text{ctrl}}$ to $\hat{\psi}_B$. In combination, the population is first reduced by α and then grows with $\hat{\psi}_B$ (Figure 1c). Substituting our rate definition (Equation 4) into this model yields additive treatment effects, $\tau_{AB} = \tau_A + \tau_B$ (see SI 1F), equivalent to the Bliss prediction derived above.

Interaction scores (μ, ν). Based on the Bliss prediction of combined treatment effects derived above, we define the Bliss interaction score μ as the normalised deviation from the prediction (Equation 6). The distribution of μ can be inferred based on the distributions of treatment effects $\boldsymbol{\tau}$ described above. For Loewe additivity, we define the interaction score ν as the deviation from dose equivalence (Equation 7). We obtain the distribution of $\boldsymbol{\nu}$ from the inverted single-drug pharmacodynamic curves $f_i^{-1}(\boldsymbol{\psi})$ (Equation S10). We then assign interaction types (synergistic, independent, antagonistic) depending on whether the 95% interval of $\boldsymbol{\mu}$ or $\boldsymbol{\nu}$ lies below, contains, or lies above zero. The resulting interaction types based on $\boldsymbol{\mu}$ and $\boldsymbol{\nu}$ for each combination are shown in Figures S4 and S5.

Disagreement between sub-inhibitory and inhibitory interaction types within reference models. Using the per-condition distributions of interaction scores described above, we next assessed whether interaction classifications remain consistent across concentration regimes. We normalised concentrations c_i by the corresponding zMIC_i (defined by $f_i(\text{zMIC}_i) = 0$; Table S1), setting $z_i = c_i/\text{zMIC}_i$. We then separately summarised inhibitory and sub-inhibitory conditions using a second, higher-level bootstrap. Specifically, we sampled conditions $(c_A, c_B)_r$ for $r = (1, \ldots, 200)$ with replacement, weighted by their mixing ratio to bias the sampling towards more equal ratios (Equation S22). For each sampled condition, we drew one estimate from the condition's distributions $\boldsymbol{\mu}(c_A, c_B)$ and $\boldsymbol{\nu}(c_A, c_B)$. To compare regimes and reference models, we define three alignment classes: agreement (same classification), soft disagreement (independent in one but synergistic or antagonistic in the other), and strong disagreement (opposite classifications). The resulting comparisons between sub-inhibitory and inhibitory regimes for $\boldsymbol{\nu}_{\text{sub}}$, $\boldsymbol{\nu}_{\text{inh}}$ and $\boldsymbol{\mu}_{\text{sub}}$, $\boldsymbol{\mu}_{\text{inh}}$ are shown in Figure 3a,b and the resulting interaction types in Table S2. Assuming Bliss independence, we observed six combinations with agreement and 9 cases of disagreement, of which one resulted in strong disagreement (AMO+PEN) and eight in soft disagreement. Assuming Loewe additivity, we observed agreement for six combinations (three of which also agreed under Bliss) and disagreement for nine combinations. Here, we observed two cases of strong disagreement (COL+TET and POL+TET) and seven with soft disagreement.

Disagreement between reference models, within concentration regimes. Figure 3c replots the same interaction summaries described above, but now compares the Bliss interaction score μ to the Loewe interaction score ν across both sub-inhibitory and inhibitory regimes in a single panel. In Figure S6a,b we show the same comparison but separated by regime. Across all 30 (2×15) comparisons, the Bliss and Loewe-based classifications agree in 14 cases, show soft disagreement in 15 cases, and show strong disagreement in one case (CHL+TET) (Figure 3c).

Interaction types can change with dose even at fixed mixing ratio. Above, we compared interaction summaries between sub-inhibitory and inhibitory regimes by aggregating condition-wise estimates across a range of doses and mixing ratios. We next ask whether interaction types also change (i) as the dose increases at a fixed mixing ratio, and (ii) as the mixing ratio varies at a fixed effect level. To facilitate both analyses, we reparameterize concentration pairs (c_A, c_B) in polar coordinates (z, ϕ), where z is the *combined dose* and ϕ is the *mixing angle* (Equation 8) that encodes the mixing

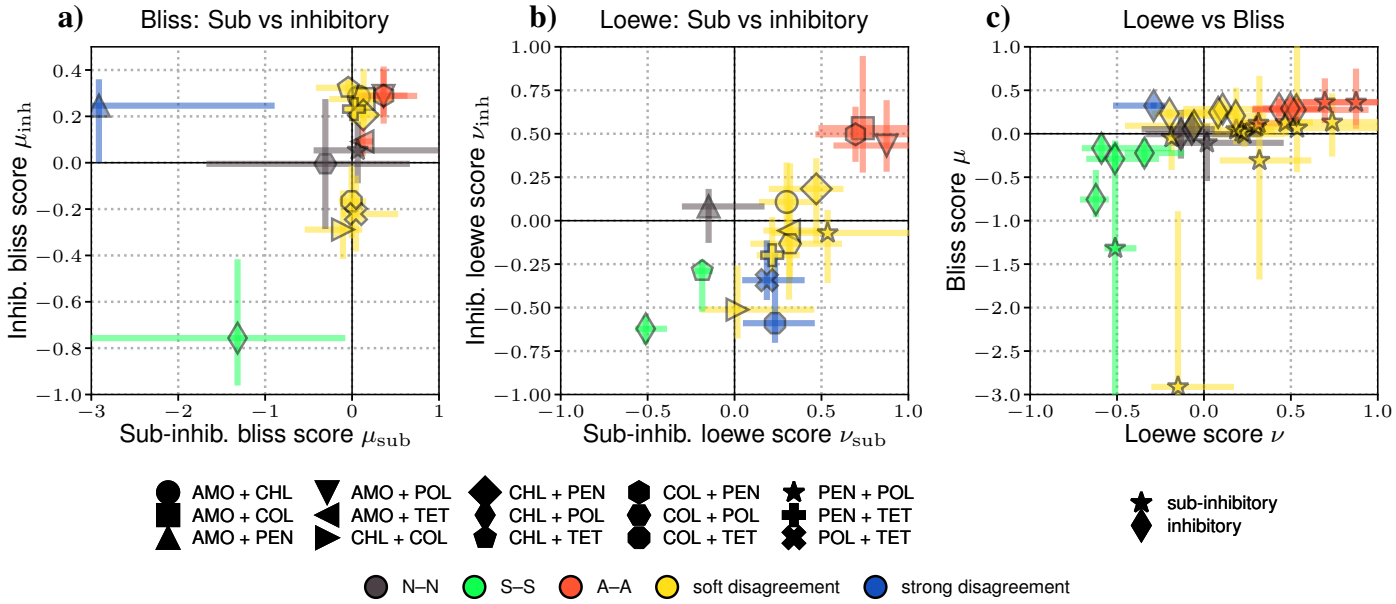

Figure 3: Interaction summaries across regimes and models. Panels **(a)** and **(b)** compare sub–inhibitory vs. inhibitory interaction scores, using **(a)** the Bliss interaction score μ and **(b)** the Loewe interaction score ν. Each point represents one drug combination, plotted as the median estimate in the sub–inhibitory regime (x-axis) against the median estimate in the inhibitory regime (y-axis), with 95% bootstrap intervals shown as horizontal and vertical error bars. **(c)** Loewe vs. Bliss comparison across regimes: each point corresponds to one combination and regime, plotted as the median Loewe interaction score ν (x-axis) against the corresponding Bliss interaction score μ (y-axis), with 95% bootstrap intervals. Markers encode the drug combination (shared legend for panels **(a)** and **(b)**), while marker shape encodes the regime in panel **(c)**. We classify interactions as synergistic (S), antagonistic (A), or independent (N; not significantly different from zero). Colors indicate interaction type agreement between the two compared axes in each panel: *agreement* if the two interaction types coincide (N–N, S–S, A–A), *soft disagreement* if one interaction type is independent and the other is non-independent (N–S, N–A), and *strong disagreement* if the classifications are opposite (S–A).

ratio.

For each drug combination, we fitted 25 continuous, monotonically decreasing surface splines on bootstrap datasets of $\psi(c_A, c_B)$ (Figure S7). Based on these splines, we estimate *polar pharmacodynamic curves*, which show ψ as a function of the combined dose z at a fixed mixing angle $\phi = 45°$ (equal mixing in units of zMIC). At a given dose, predicted values above the observed ψ indicate synergy, whereas predicted values below the observed ψ indicate antagonism. For both reference models, there are examples where the interaction changes direction as the combined dose increases. For the combination AMO+COL (Figure 4a), the Loewe-based interaction shifts from antagonism at lower doses to synergy at higher doses. For AMO+PEN (Figure 4b) Bliss-based interaction flips, with synergy at lower doses and strong antagonism at higher doses. *Polar pharmacodynamic curves* at 45° for all combinations are shown in Figure S8.

Interaction types can depend on the mixing ratio. To assess whether interaction types depend on the mixing ratio at a fixed effect level, we extracted isoboles from the median surface spline, i.e., the path $(z, \phi)_i$ along which the time-weighted net growth rate is constant ($\psi_i = 0\,\frac{1}{\mathrm{h}}$; Figure S9). Along each isobole, we evaluate Bliss- and Loewe-based predictions and plot these predictions as a function of ϕ. For many combinations, the inferred interaction type is stable across ϕ, as exemplified by CHL+TET (Figure 4c). However, combinations showing mixing-ratio dependence are also common, as exemplified for COL+PEN (Figure 4d). Plots for all combinations are shown in Figure S10.

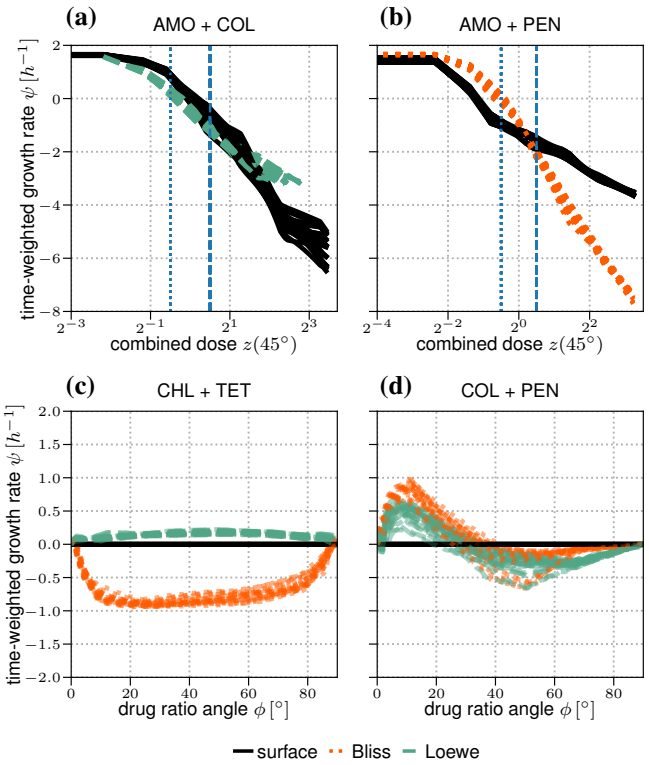

Figure 4: Panels (a,b) show *polar pharmacodynamic curves* at $\phi = 45°$ (corresponding to a 1:1 ratio in units of zMIC) for (a) AMO+COL and (b) AMO+PEN. The x-axis shows the combined dose z, where $z = 1/\sqrt{2}$ (blue dotted line) corresponds to both single-drug doses equaling 0.5 zMIC, and $z = \sqrt{2}$ (blue dashed line) corresponds to both equaling 1 zMIC. Panels (c,d) show the Bliss- and Loewe-based predictions for ψ over the mixing angle ϕ along the observed isobole at $\psi = 0\,\frac{1}{\mathrm{h}}$ for (c) COL+PEN and (d) CHL+TET.

Discussion

We quantified interaction patterns across a wide concentration range for several drug combinations with different modes of action. Quantifying the size of the bacterial population is notoriously difficult because bacterial death has many facets, and no single method captures all of them [44, 45]. In this work, we used bioluminescence as a proxy for population size. This choice enabled us to record 8640 finely time-resolved (every 10 minutes for five hours) growth trajectories at high throughput. Bioluminescence has been shown to be a better proxy for biomass than for cell number [45], which makes interpreting our readout as biomass the more robust interpretation. However, since we restricted our analysis to drugs for which changes in biomass align with changes in cell number (i.e. limited filamentation) [45], we do not expect qualitatively different conclusions when using an alternative readout of population size.

For many of the observed trajectories treated with higher concentrations of polymyxins (COL and POL), the light intensity dropped below the detection limit within the first few minutes. In principle, slope-based estimates can still be inferred for such curves. However, comparing these estimates across drugs with different onsets and durations of treatment effects is conceptually difficult to justify. To enable fair comparisons across drugs, we therefore used a weighted growth measure integrated over a shared timeframe that is equal for all trajectories ($T \approx 2\,\mathrm{h}$). However, this choice comes at the cost of having to discard all trajectories that fall below the detection limit too early.

To investigate how different treatment dynamics combine, we developed a simplified antibiotic–peptide interaction model. This model predicts that combinations of a short-acting, peptide-like drug with a drug with time-invariant treatment effects should follow Bliss independence. The observed isoboles for peptide–non-peptide pairs in Figure S9 confirm this behaviour, as they were closer to the Bliss-based prediction than to the Loewe-based prediction for all pairs except COL+PEN.

To address our core question — how predictive sub-MIC interaction patterns are for inhibitory interactions — we aggregated interaction estimates for sub-inhibitory and inhibitory conditions and compared them. For both reference models (Bliss independence and Loewe additivity), more than half of the combinations showed soft disagreement between inhibitory and sub-inhibitory regimes, i.e., a significant synergy or antagonism in one regime but not in the other. This does not necessarily imply that sub-inhibitory measures are uninformative, because non-significance of synergistic/antagonistic interactions is not evidence of independence and can arise from variance. Such variance can result from aggregating across diverse conditions and mixing ratios, which we showed can influence the interaction type (Figure S10). Importantly, for both reference models, we observed more cases of synergistic or antagonistic agreement than strong disagreement, indicating that sub-inhibitory interaction measures retain some qualitative predictive value.

Our results also confirm the practical limitations of Loewe-based interaction measures at high concentrations that have been reported previously ([46]). Since Loewe relies on the inverse of the single-drug pharmacodynamic functions, it is only defined when the combined effect lies within the effect ranges spanned by both single-drug treatments. For drug pairs with very different maximal killing rates, this condition fails in large parts of the checkerboard (see undefined regions in Figure S5). This is a severe limitation that prohibits the quantification of drug interactions for a large number of therapeutically relevant conditions. Consistent with previous work (e.g. [47]), we found that the Bliss and Loewe frameworks can produce opposite classifications.

Our findings show that conclusions about synergy or antagonism depend on the concentration range, mixing ratio, and the reference model on the basis of which synergy or antagonism is determined. Accordingly, single-point measurements at a single sub-inhibitory concentration are insufficient to reliably characterise drug interactions at clinically relevant inhibitory concentrations.

Methods

Strains and Media. We used the bioluminescent strain *Escherichia coli* MG1655 ΔgalK::(kan^R-luxCDABE) constructed previously [45]. Cultures were grown in LB medium (Sigma L3022).

Drug preparation. We explored drug interactions among six drugs (Table 1), resulting in 15 drug–drug pairs. For each pair, one compound was designated drug A and the other drug B. Each compound was prepared as a $\times 20$ stock of its highest working concentration. We then performed a twofold dilution series in a 12-column deepwell plate, resulting in 11 diluted concentrations and one drug-free column. For drug A, we transferred 125 µL per well into a 96-well plate (subreservoir A) with a horizontal concentration gradient. For drug B, we transferred 50 µL per well into two 96-well plates (antibiotic reservoir plates I and II) with vertical concentration gradients (each 6×12 layout). All plates were stored at $-80\,^{\circ}\mathrm{C}$ to minimise degradation over time, accepting a one-time freeze–thaw-related degradation.

Dose response assays. For each assay, we prepared four overnight cultures grown for 14 h. Cultures were distributed to fill an entire 384-well source plate (Greiner 781073), so that the replicates formed a 2×2 block format (e.g. C1–rep1, C2–rep2, D1–rep3, D2–rep4). We then prefilled two

Table 1: Drugs used in the experiments, the solvent, the estimated zMIC (by fitting the single-drug pharmacodynamic curves), and the supplier with catalogue number.

drug	solvent	zMIC [$\frac{\mu g}{mL}$]	supplier
amoxicillin (AMO)	water	8.42	ThermoFischer, J61290.14
chloramphenicol (CHL)	DMSO	54.11	Sigma, C0378
colistin (COL)	water	0.58	Sigma, C4461
penicillin (PEN)	water	153.86	Roth, HP48.2
polymyxin B (POL)	water	0.51	Roth, 0235.1
tetracycline (TET)	DMSO	15.15	Sigma, T3383

white 384-well assay plates (Greiner 781073) with 54 µL LB per well and transferred inocula from the source plate to both assay plates (I, II) using an Evo 200 liquid handling platform (Tecan) with a pintool. The dilution is approximately 1:150, although we observed substantial well-to-well variation in the effective inoculum size (see below). Plates were incubated for 2 h to reach exponential phase. Simultaneously, subreservoir A and both antibiotic-reservoir plates were thawed. 50 µL from each well of the subreservoir A were transferred to the corresponding wells of both antibiotic-reservoir plates, generating a 10 x mixture of drugs A and B. For both assay plates, the assay started as follows: a baseline luminescence reading was taken, 6 µL of the 10 x drug mixture was added (defining $t = 0$ at dosing for the respective wells), and a second luminescence reading was taken. Subsequently, we alternated between reading assay plates I and II for a total duration of 5 h. Luminescence was recorded with an Infinite F200 plate reader (Tecan) using a 250 ms integration time.

Data preprocessing. To estimate stray.light contamination, we conducted a calibration experiment in which six source wells (E5, E12, E20, L5, L12, L20) contained stationary-phase cultures while all other wells remained empty. From a single luminescence read of the full plate, we constructed a distance-dependent stray-light kernel (Figure S11) and corrected each well by subtracting the summed contributions from neighbouring wells (restricted to distances $d \leq 3$, Equation S8). We defined the lower limit of detection as $I_{\mathrm{LoD}} = 10\,\mathrm{RLU}$ and the upper limit of detection as $10^6\,\mathrm{RLU}$. We defined the common analysis horizon T as the earliest time point at which any untreated control well exceeded the upper detection limit, yielding $T \approx 2\,\mathrm{h}$. For each well, we computed the fraction of observations up to T below I_{LoD}. Wells with more than 20% of observations below I_{LoD} were excluded from all subsequent analyses. For retained wells, values below I_{LoD} were censored by replacing them with I_{LoD}. For numerical integration, we interpolated the log-normalised signal to obtain values on the shared horizon $t = T$ (see also SI 1B).

Time-weighted net growth rate. We define ψ as the linearly time-weighted net growth rate (SI: Equation S1) over the common time horizon T. We infer ψ by calculating the scaled area under the log-normalised light intensity $Y(t) = \ln\big(I(t)/I(0)\big)$ (SI: Equation S2, Equation S3),

$$\psi = \frac{2}{T^2}\int_0^T Y(t)\,\mathrm{d}t. \tag{4}$$

Classification of inhibitory and sub-inhibitory conditions. We classify each checkerboard condition as inhibitory, sub-inhibitory, or not significantly different from zero by testing whether replicate time-weighted growth-rate estimates $\psi(c_A, c_B)$ are consistently positive or negative. With four replicates, the binomial probability of observing all positive (or all negative) signs with equal probability is $0.5^4 = 0.0625$. This classification is used to annotate the ψ heatmaps (Figure 2, Figure S3) and to define inhibitory and sub-inhibitory regime pools.

Single-drug pharmacodynamic curve fitting. For each drug, we aggregated all single-drug data across experiments and fitted pharmacodynamic curves $f(c)$ to the corresponding time-weighted growth-rate estimates ψ:

$$f(c) = \psi_0 - \frac{(\psi_0 - \psi_{\min})(c/\mathrm{zMIC})^{\kappa}}{(c/\mathrm{zMIC})^{\kappa} - (\psi_{\min}/\psi_0)}, \quad [0,\infty) \to [\psi_{\min}, \psi_0] \tag{5}$$

Here, ψ_0 denotes the maximum and $\psi_{\min}$ the minimum time-weighted growth rate, corresponding to $c = 0$ and $c \to \infty$, respectively. κ denotes the Hill coefficient and zMIC the concentration at which $f(\mathrm{zMIC}) = 0$. The model parameters psi_0, $\psi_{\min}$, κ, zMIC were jointly estimated by least-squares fitting of Equation 5.

Distribution of treatment effects. We define the treatment effect τ as the linearly time-weighted average difference between the untreated and treated instantaneous net growth rates over the common time horizon T (SI: Equation S6). Equivalently, τ is the scaled area between the control and treatment trajectories on the log-normalised scale (illustrated in Figure 1b). Because τ is a comparative measure between one untreated and one treated trajectory, we bootstrap treated–control well pairs with replacement ($B = 200$; details in SI 1G). For each condition (c_A, c_B) and draw b, we compute $\tau_b(c_A, c_B) = \psi_b(\emptyset) - \psi_b(c_A, c_B)$, yielding the distribution of treatment effects $\boldsymbol{\tau}(c_A, c_B)$. Throughout this manuscript, distributions are denoted by bold symbols. We classify such bootstrap distributions as significant if the central 95% bootstrap interval excludes zero, and as not significant otherwise.

Bliss-based interaction score μ. We define the Bliss based interaction score as the normalised deviation from the Bliss-prediction for combined treatment effects (see SI 1D and Equation 3):

$$\mu_b(c_A, c_B) = \frac{\tau_b(c_A) + \tau_b(c_B) - \tau_b(c_A, c_B)}{\mathrm{median}\big(\boldsymbol{\tau}(c_A)\big) + \mathrm{median}\big(\boldsymbol{\tau}(c_B)\big)}. \tag{6}$$

To avoid misinterpreting noise as interaction, we only evaluate $\nu(c_A, c_B)$ if $\boldsymbol{\tau}(c_A, c_B)$ is significantly greater than zero and at least one of $\boldsymbol{\tau}(c_A)$ or $\boldsymbol{\tau}(c_B)$ is significantly greater than zero.

Loewe-based interaction score ν. We define a Loewe interaction score (details in SI 1E) that quantifies deviations from dose equivalence as

$$\nu_b(c_A, c_B) = \frac{c_A}{f_A^{-1}\big(\psi_b(c_A, c_B)\big)} + \frac{c_B}{f_B^{-1}\big(\psi_b(c_A, c_B)\big)} - 1. \tag{7}$$

Here f_i denotes a pharmacodynamic function mapping concentration to net growth, $f_i(c) = \psi$. The inverse $f_i^{-1}(\psi)$ is the corresponding single-drug equivalent concentration of drug i. Our definition of ν is analogous to the combination index $(\mathrm{CI} - 1)$ [36], but uses a different pharmacodynamic model f_i (either Equation S10 or inferred numerically from the single-drug edges of the surface splines). To avoid misinterpreting noise as interaction, we only evaluate $\nu(c_A, c_B)$ if $\boldsymbol{\tau}(c_A, c_B)$ is significantly greater than zero and at least one of $\boldsymbol{\tau}(c_A)$ or $\boldsymbol{\tau}(c_B)$ is significantly greater than zero.

Polar reparametrization. We normalise concentrations of drug i using the corresponding zMIC_i estimates obtained from pharmacodynamic curve fits (Table 1): $z_i = c_i/\mathrm{zMIC}_i$. We then define polar coordinates based on the normalised concentrations:

$$z = \sqrt{z_A^2 + z_B^2}, \qquad \phi = \arctan 2\big(z_B, z_A\big), \tag{8}$$

with ϕ corresponding to the *mixing angle* and z to the *combined dose*. These coordinates were used to plot polar pharmacodynamic curves, which show the treatment effect over the combined dose z for a fixed mixing angle ϕ. These curves represent cross-sections through the surface splines at fixed ϕ.

Inoculum effects. We noticed a much larger-than-expected variation in pre-treatment light intensity I_0 in our data, which we use as a proxy for inoculum size. To assess the impact of this variation on the results, we regressed ψ for each single-drug and concentration on the pre-treatment signal I_0 (SI 1I). We found negligible inoculum effects for AMO, CHL, PEN, and TET, but substantial effects for COL and POL at intermediate concentrations (see Figure S12). Because the size of the inoculum did not show a significant directional trend along the concentration index ($p = 0.092$), the variance of the inoculum mainly adds noise at intermediate concentrations of COL and POL, contributing to an increased scatter in Figure S2c,e.

Data, Materials, and Software Availability

Experimental datasets and code are available at Zenodo (DOI: 10.5281/zenodo.18374151).

Acknowledgements

We thank ETH Zurich for funding this work. During manuscript preparation, we used OpenAI's ChatGPT for editorial assistance (coding, grammar, and proofreading).

Bibliography

1. Mohsen Naghavi et al. Global burden of bacterial antimicrobial resistance 1990–2021: a systematic analysis with forecasts to 2050. *The Lancet*, 404(10459):1199—-1226, 2024. doi: 10.1016/S0140-6736(24)01867-1.
2. Christopher Witzany et al. Is antimicrobial resistance evolution accelerating? *PLOS Pathogens*, 16(10):e1008905, 2020. doi: 10.1371/journal.ppat.1008905.
3. Roy M. Gulick et al. Treatment with indinavir, zidovudine, and lamivudine in adults with human immunodeficiency virus infection and prior antiretroviral therapy. *New England Journal of Medicine*, 337(11):734—-739, 1997. doi: 10.1056/NEJM199709113371102.
4. Daniel E. Goldberg et al. Outwitting evolution: Fighting drug-resistant tb, malaria, and hiv. *Cell*, 148(6):1271—-1283, 2012. doi: 10.1016/j.cell.2012.02.021.
5. Sebastian Bonhoeffer et al. Evaluating treatment protocols to prevent antibiotic resistance. *Proceedings of the National Academy of Sciences*, 94(22):12106—-12111, 1997. doi: 10.1073/pnas.94.22.12106.
6. Burcu Tepekule et al. Modeling antibiotic treatment in hospitals: A systematic approach shows benefits of combination therapy over cycling, mixing, and mono-drug therapies. *PLOS Computational Biology*, 13(9):e1005745, 2017. doi: 10.1371/journal.pcbi.1005745.
7. Hildegard Uecker et al. Antibiotic treatment protocols revisited: the challenges of a conclusive assessment by mathematical modelling. *Journal of The Royal Society Interface*, 18 (181), 2021. doi: 10.1098/RSIF.2021.0308.
8. Daniel C. Angst et al. Comparing treatment strategies to reduce antibiotic resistance in an in vitro epidemiological setting. *Proceedings of the National Academy of Sciences*, 118(13), 2021. doi: 10.1073/PNAS.2023467118.
9. Malte Muetter et al. The impact of treatment strategies on the epidemiological dynamics of plasmid-conferred antibiotic resistance. *Proceedings of the National Academy of Sciences*, 121(52), 2024. doi: 10.1073/PNAS.2406818121.
10. Berit Siedentop et al. The effect of combining antibiotics on resistance: A systematic review and meta-analysis. *Elife*, 2024. doi: 10.7554/eLife.93740.1.
11. Julie Foucquier et al. Analysis of drug combinations: current methodological landscape. *Pharmacology Research & Perspectives*, 3(3), 2015. doi: 10.1002/PRP2.149.
12. Diana Duarte et al. Evaluation of synergism in drug combinations and reference models for future orientations in oncology. *Current Research in Pharmacology and Drug Discovery*, 3: 100110, 2022. doi: 10.1016/J.CRPHAR.2022.100110.
13. C. I. BLISS et al. The toxicity of poisons applied jointly. *Annals of Applied Biology*, 26(3): 585—-615, 1939. doi: 10.1111/j.1744-7348.1939.tb06990.x.
14. S. Loewe et al. Über kombinationswirkungen. *Archiv für Experimentelle Pathologie und Pharmakologie*, 114(5-6):313—-326, 1926. doi: 10.1007/BF01952257.
15. Desiree Y. Baeder et al. Antimicrobial combinations: Bliss independence and loewe additivity derived from mechanistic multi-hit models. *Philosophical Transactions of the Royal Society B: Biological Sciences*, 371(1695):20150294, 2016. doi: 10.1098/rstb.2015.0294.
16. Wilhelm Frei et al. Versuche über kombination von desinfektionsmitteln. *Zeitschrift für Hygiene und Infektionskrankheiten*, 75(1):433—-496, 1913. doi: 10.1007/BF02207053.
17. Pamela Yeh et al. Functional classification of drugs by properties of their pairwise interactions. *Nature Genetics*, 38(4):489—-494, 2006. doi: 10.1038/ng1755.
18. E. M. O'Shaughnessy et al. Antifungal interactions within the triple combination of amphotericin b, caspofungin and voriconazole against aspergillus species. *Journal of Antimicrobial Chemotherapy*, 58(6):1168—-1176, 2006. doi: 10.1093/JAC/DKL392.
19. Guillaume Chevereau et al. Quantifying the determinants of evolutionary dynamics leading to drug resistance. *PLOS Biology*, 13(11):e1002299, 2015. doi: 10.1371/journal.pbio.1002299.
20. D. Russ et al. Additivity of inhibitory effects in multidrug combinations. *Nature Microbiology*, 3(12):1339—-1345, 2018. doi: 10.1038/s41564-018-0252-1.
21. Itay Katzir et al. Prediction of ultra-high-order antibiotic combinations based on pairwise interactions. *PLOS Computational Biology*, 15(1):e1006774, 2019. doi: 10.1371/journal.pcbi.1006774.
22. Bor Kavčič et al. Mechanisms of drug interactions between translation-inhibiting antibiotics. *Nature Communications*, 11(1), 2020. doi: 10.1038/s41467-020-17734-z.
23. Chiara Rezzoagli et al. Combining antibiotics with antivirulence compounds can have synergistic effects and reverse selection for antibiotic resistance in pseudomonas aeruginosa. *PLOS Biology*, 18(8):e3000805, 2020. doi: 10.1371/JOURNAL.PBIO.3000805.
24. D. L. Sánchez-Hevia et al. Sublethal interaction factor (sif), a growth-based method to analyze antibiotic combinations at sub-inhibitory concentrations. *Microbiology Spectrum*, 13(12), 2025. doi: 10.1128/SPECTRUM.01070-25.
25. Natalie Ann Lozano-Huntelman et al. The evolution of resistance to synergistic multi-drug combinations is more complex than evolving resistance to each individual drug component. *Evolutionary Applications*, 16(12):1901—-1920, 2023. doi: 10.1111/eva.13608.
26. Bing Yang et al. Combination susceptibility testing of common antimicrobials in vitro and the effects of sub-mic of antimicrobials on staphylococcus aureus biofilm formation. *Frontiers in Microbiology*, 8, 2017. doi: 10.3389/FMICB.2017.02125.
27. Serge Ruden et al. Synergy pattern of short cationic antimicrobial peptides against multidrug-resistant pseudomonas aeruginosa. *Frontiers in Microbiology*, 10, 2019. doi: 10.3389/FMICB.2019.02740.
28. Jia-Feng Liu et al. Interaction tolerance detection test for understanding the killing efficacy of directional antibiotic combinations. *mBio*, 13(1), 2022. doi: 10.1128/MBIO.00004-22.
29. Paolo S. Ocampo et al. Antagonism between bacteriostatic and bactericidal antibiotics is prevalent. *Antimicrobial Agents and Chemotherapy*, 58(8):4573—-4582, 2014. doi: 10.1128/AAC.02463-14.
30. G.G. Rao et al. Assessment and modelling of antibacterial combination regimens. *Clinical Microbiology and Infection*, 24(7):689—-696, 2018. doi: 10.1016/j.cmi.2017.12.004.
31. Guozhi Yu et al. Combination effects of antimicrobial peptides. *Antimicrobial Agents and Chemotherapy*, 60(3):1717—-1724, 2016. doi: 10.1128/AAC.02434-15.
32. Veronica Rico Caballero et al. Efficacy of human-simulated exposures of ceftolozane-tazobactam alone and in combination with amikacin or colistin against multidrug-resistant pseudomonas aeruginosa in an *In Vitro* pharmacodynamic model. *Antimicrobial Agents and Chemotherapy*, 62(5), 2018. doi: 10.1128/AAC.02384-17.
33. Iris H. Chen et al. Imipenem/cilastatin/relebactam alone and in combination against *Pseudomonas aeruginosa* in the *In Vitro* pharmacodynamic model. *Antimicrobial Agents and Chemotherapy*, 64(12), 2020. doi: 10.1128/AAC.01764-20.
34. Bence Bognár et al. Drug combinations targeting antibiotic resistance. *npj Antimicrobials and Resistance*, 2(1), 2024. doi: 10.1038/S44259-024-00047-2.
35. Guozhi Yu et al. Predicting drug resistance evolution: insights from antimicrobial peptides and antibiotics. *Proceedings of the Royal Society B: Biological Sciences*, 285(1874): 20172687, 2018. doi: 10.1098/rspb.2017.2687.
36. Ting-Chao Chou et al. Quantitative analysis of dose-effect relationships: the combined effects of multiple drugs or enzyme inhibitors. *Advances in Enzyme Regulation*, 22:27—-55, 1984. doi: 10.1016/0065-2571(84)90007-4.
37. Joseph Meletiadis et al. Concentration-dependent synergy and antagonism within a triple antifungal drug combination against *Aspergillus* species: Analysis by a new response surface model. *Antimicrobial Agents and Chemotherapy*, 51(6):2053—-2064, 2007. doi: 10.1128/AAC.00873-06.
38. Bor Kavčič et al. Minimal biophysical model of combined antibiotic action. *PLOS Computational Biology*, 17(1):e1008529, 2021. doi: 10.1371/JOURNAL.PCBI.1008529.
39. Roland R. Regoes et al. Pharmacodynamic functions: a multiparameter approach to the design of antibiotic treatment regimens. *Antimicrobial Agents and Chemotherapy*, 48(10): 3670—-3676, 2004. doi: 10.1128/AAC.48.10.3670-3676.2004.
40. Guillaume Chevereau et al. Systematic discovery of drug interaction mechanisms. *Molecular Systems Biology*, 11(4), 2015. doi: 10.15252/msb.20156098.
41. S Andreas Angermayr et al. Growth-mediated negative feedback shapes quantitative antibiotic response. *Molecular Systems Biology*, 18(9), 2022. doi: 10.15252/msb.202110490.
42. A. MacGowan et al. Assessment of different antibacterial effect measures used in in vitro models of infection and subsequent use in pharmacodynamic correlations for moxifloxacin. *Journal of Antimicrobial Chemotherapy*, 46(1):73—-78, 2000. doi: 10.1093/JAC/46.1.73.

43. Justin R. Lenhard et al. Evolution of staphylococcus aureus under vancomycin selective pressure: the role of the small-colony variant phenotype. *Antimicrobial Agents and Chemotherapy*, 59(2):1347—-1351, 2015. doi: 10.1128/AAC.04508-14.
44. Renfei Wu et al. Bacterial killing and the dimensions of bacterial death. *npj Biofilms and Microbiomes*, 10(1), 2024. doi: 10.1038/s41522-024-00559-9.
45. Malte Muetter et al. High-throughput quantification of population dynamics using luminescence. *Elife*, 2026. doi: 10.7554/eLife.109213.1.
46. Christian T. Meyer et al. Quantifying drug combination synergy along potency and efficacy axes. *Cell Systems*, 8(2):97—-108.e16, 2019. doi: 10.1016/j.cels.2019.01.003.
47. Anna H.C. Vlot et al. Applying synergy metrics to combination screening data: agreements, disagreements and pitfalls. *Drug Discovery Today*, 24(12):2286—-2298, 2019. doi: 10.1016/J.DRUDIS.2019.09.002.